ChemPubSoc Europe

DOI: 10.1002/chem.201903897

CHEMISTRY A European Journal Full Paper

Nitrides

Solid Solutions of Grimm–Sommerfeld Analogous Nitride Semiconductors II-IV-N_2 (II = Mg, Mn, Zn; IV = Si, Ge): Ammonothermal Synthesis and DFT Calculations

Mathias Mallmann,[a] Robin Niklaus,[a] Tobias Rackl,[a] Maximilian Benz,[a] Thanh G. Chau,[a] Dirk Johrendt,[a] Ján Minár,[b] and Wolfgang Schnick*[a]

Dedicated to Professor Hans-Jörg Deiseroth on the Occasion of his 75th birthday

Abstract: Grimm–Sommerfeld analogous II-IV-N_2 nitrides such as $ZnSiN_2$, $ZnGeN_2$, and $MgGeN_2$ are promising semiconductor materials for substitution of commonly used (Al,Ga,In)N. Herein, the ammonothermal synthesis of solid solutions of II-IV-N_2 compounds (II = Mg, Mn, Zn; IV = Si, Ge) having the general formula $(II^a_{1-x}II^b_x)$-IV-N_2 with $x \approx 0.5$ and ab initio DFT calculations of their electronic and optical properties are presented. The ammonothermal reactions were conducted in custom-built, high-temperature, high-pressure autoclaves by using the corresponding elements as starting materials. $NaNH_2$ and KNH_2 act as ammonobasic mineralizers that increase the solubility of the reactants in supercritical ammonia. Temperatures between 870 and 1070 K and pressures up to 200 MPa were chosen as reaction conditions. All solid solutions crystallize in wurtzite-type superstructures with space group $Pna2_1$ (no. 33), confirmed by powder XRD. The chemical compositions were analyzed by energy-dispersive X-ray spectroscopy. Diffuse reflectance spectroscopy was used for estimation of optical bandgaps of all compounds, which ranged from 2.6 to 3.5 eV (Ge compounds) and from 3.6 to 4.4 eV (Si compounds), and thus demonstrated bandgap tunability between the respective boundary phases. Experimental findings were corroborated by DFT calculations of the electronic structure of pseudorelaxed mixed-occupancy structures by using the KKR + CPA approach.

Introduction

The investigation of new semiconducting materials is of essential importance due to the increasing demand and the large number of possible applications. At present, GaN and solid solutions of group 13 nitrides (Al,Ga,In)N are the most important (opto)electronic semiconductors with different application fields in modern electronic technologies. These include areas such as light-emitting diodes, field-effect transistors, and laser diodes.[1,2] By using solid solutions of group 13 nitrides, a large bandgap range from around 0.7 to 6.2 eV can be covered.[3] However, the major problem of these compounds arises from the limited availability of the constituent elements. Ga and In only arise as byproducts during the production of copper, aluminum, lead, and zinc and are therefore difficult to access. In contrast, the natural abundance of elements such as Zn or Si is considerably higher. Therefore, one goal of modern semiconductor research is to synthesize compounds composed of earth-abundant elements. Recently, DFT calculations indicated various zinc nitrides such as Grimm–Sommerfeld analogous Zn(Si,Ge,Sn)N_2 compounds as possible next-generation semiconductors.[4] These materials exhibit similar electronic and optical properties to GaN, including high carrier mobility and small carrier effective masses, as well as high chemical stability and dopability. Additionally, such II-IV-N_2 compounds show lattice parameters similar to those of (Al,Ga,In)N, which enable the formation of hybrid structures or epitaxial growth on group 13 nitrides. In the last few years, different studies examined the synthesis and properties of II-IV-N_2 compounds.[5–10] However, the bulk synthesis of these materials is still challenging. Recently, we employed the ammonothermal method as a suitable synthetic approach to Zn-IV-N_2 compounds (IV = Si, Ge), as well as other Grimm–Sommerfeld analogous nitrides such as II-IV-N_2 (II = Mg, Mn; IV = Si, Ge), II_2-P-N_3 (II = Mg, Zn), $CaGaSiN_3$, and $Ca_{1-x}Li_xAl_{1-x}Ge_{1+x}N_3$ ($x \approx 0.2$).[11–15] By employing this method, we were able to synthesize crystalline $ZnSiN_2$ and $ZnGeN_2$ with crystal sizes of several micrometers and, for the

[a] M. Mallmann, R. Niklaus, T. Rackl, M. Benz, T. G. Chau, Prof. Dr. D. Johrendt, Prof. Dr. W. Schnick
Department of Chemistry, University of Munich (LMU)
Butenandtstrasse 5-13 (D), 81377 Munich (Germany)
E-mail: wolfgang.schnick@uni-muenchen.de

[b] Prof. Dr. J. Minár
New Technologies Research Centre
University of West Bohemia, Univerzitni 8, 30614 Pilsen (Czech Republic)

Supporting information and the ORCID identification number(s) for the author(s) of this article can be found under: https://doi.org/10.1002/chem.201903897.

first time, single crystals of Mg_2PN_3 with lengths of up to 30 μm. Furthermore, well-defined crystallites of InN were obtained ammonothermally quite recently, indicating the ammonothermal process as an auspicious method for synthesis and crystal growth of semiconducting nitrides.[16]

Herein, we present the synthesis of the solid solutions $Mg_{1-x}Mn_xSiN_2$, $Mg_{1-x}Zn_xSiN_2$, $Mn_{1-x}Zn_xSiN_2$, $Mg_{1-x}Mn_xGeN_2$, $Mg_{1-x}Zn_xGeN_2$, and $Mn_{1-x}Zn_xGeN_2$ ($x \approx 0.5$) under ammonothermal conditions. The Si compounds were synthesized at 1070 K and pressures up to 150 MPa, whereas the Ge compounds already decompose at such high temperatures and were therefore synthesized at 870 K and maximum pressures of up to 200 MPa. The products were analyzed by powder X-ray diffraction (PXRD) and energy-dispersive X-ray spectroscopy (EDX). Diffuse reflectance spectroscopy and DFT calculations were used for evaluation of optical and electronic properties. Due to the mixed-occupancy sites in solid solutions, DFT calculations are challenging without relying on extensive supercell calculations. Previous works on mixed-occupancy $CaMSiN_3$ (M = Al, Ga) materials and fully ordered II-IV-N_2 materials were successfully used to describe the electronic structure in the framework of the Korringa–Kohn–Rostoker (KKR) Green's function method together with bandgap corrections by the Engel–Vosko formalism.[12,17] Here we advance the described method to show successful application to solid solutions of these nitride materials. The presented results again demonstrate the great potential of the ammonothermal approach for synthesis of semiconducting materials and mark another step of II-IV-N_2 compounds towards next-generation semiconductors as alternatives for commonly used group 13 nitrides.

Results and Discussion

Synthesis

The solid solutions of II-IV-N_2 compounds $Mg_{1-x}Mn_xSiN_2$, $Mg_{1-x}Zn_xSiN_2$, $Mn_{1-x}Zn_xSiN_2$, $Mg_{1-x}Mn_xGeN_2$, $Mg_{1-x}Zn_xGeN_2$, and $Mn_{1-x}Zn_xGeN_2$ ($x \approx 0.5$) were synthesized by using supercritical ammonia as solvent in custom-built, high-pressure, high-temperature autoclaves. The respective elements (Mg, Mn, Zn, Ge, and Si) were used as starting materials. NaN_3 (Ge compounds) and KN_3 (Si compounds) were added to the reaction mixture. They decompose during the reaction and form the corresponding amides ($NaNH_2$ and KNH_2), which act as ammonobasic mineralizers. The azides were used instead of metals or amides because of their high purity and chemical stability towards hydrolysis. The mineralizers increase the solubility of the other starting materials in supercritical ammonia by formation of soluble intermediates (e.g., $K_2[Zn(NH_2)_4]$).[18,19] In the case of the Si compounds, the use of KNH_2 instead of $NaNH_2$ resulted in products with higher crystallinity. These findings are consistent with previous reports in which $MgSiN_2$ and $MnSiN_2$ were synthesized with KNH_2, and $MgGeN_2$ and $MnGeN_2$ with $NaNH_2$.[12] Due to the preferred formation of intermediates around 700 K and the following transformation into the nitrides at higher temperatures, the syntheses were conducted in two temperature steps (see Experimental Section).

Whereas all Si compounds were synthesized at 1070 K with an autogenous pressure of around 150 MPa, Ge-containing compounds are thermally less stable and already decompose at these temperatures. Therefore, $Mg_{1-x}Mn_xGeN_2$, $Mg_{1-x}Zn_xGeN_2$ and $Mn_{1-x}Zn_xGeN_2$ ($x \approx 0.5$) were synthesized at 870 K and maximum pressures of about 200 MPa. To prevent uncontrolled diffusion of the starting materials through the autoclave, the reaction mixtures were contained in closed Ta liners. The lids of the liners contain a small hole to ensure filling with ammonia. After reaction, residual amides and other impurity phases were removed as far as possible (see below) by washing the products with ethanol and acetic acid. Optical micrographs of the products are shown in Figure 1.

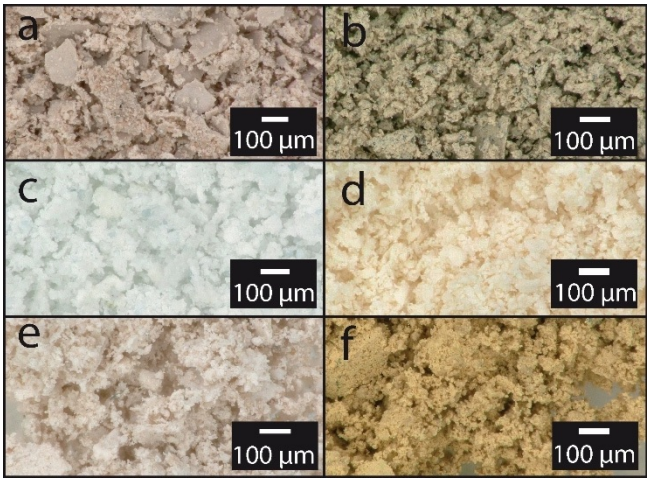

Figure 1. Optical micrographs of $Mg_{1-x}Mn_xSiN_2$ (a), $Mg_{1-x}Mn_xGeN_2$ (b), $Mg_{1-x}Zn_xSiN_2$ (c), $Mg_{1-x}Zn_xGeN_2$ (d), $Mn_{1-x}Zn_xSiN_2$ (e), and $Mn_{1-x}Zn_xGeN_2$ (f) with $x \approx 0.5$.

Crystal structure

The purified compounds were analyzed by PXRD. Rietveld plots of all products are shown in Figure 2. Wyckoff positions, atomic coordinates, and lattice parameters as starting values for the refinement were taken from ammonothermally synthesized II-IV-N_2 phases in the literature.[11,12] Obtained crystallographic data are summarized in Table 1, and refined atomic coordinates and displacement parameters in Tables S1–S6 in the Supporting Information. All compounds crystallize in orthorhombic space group $Pna2_1$ (no. 33) and can be derived from the wurtzite structure type ($P6_3mc$, no. 186) by ordering of tetrahedrally coordinated divalent and tetravalent cations to form *sechser* rings along [001] (Figure 3).[20] The ordering can be verified by the expected (011) and (110) superstructure reflections for the orthorhombic structure,[21] which occur as the first two reflections of the target phases in the powder patterns. Further ordering of the different divalent cations in the solid solutions (e.g., Mg^{2+} and Zn^{2+} in $Mg_{1-x}Zn_xGeN_2$) could not be detected by PXRD. The occupation of the divalent cation positions were refined and slightly deviate from 0.5 for each divalent cation (see Supporting Information Tables S1–S6). The largest deviation is found in $Mg_{0.375}Mn_{0.625}GeN_2$, whereas the deviations of

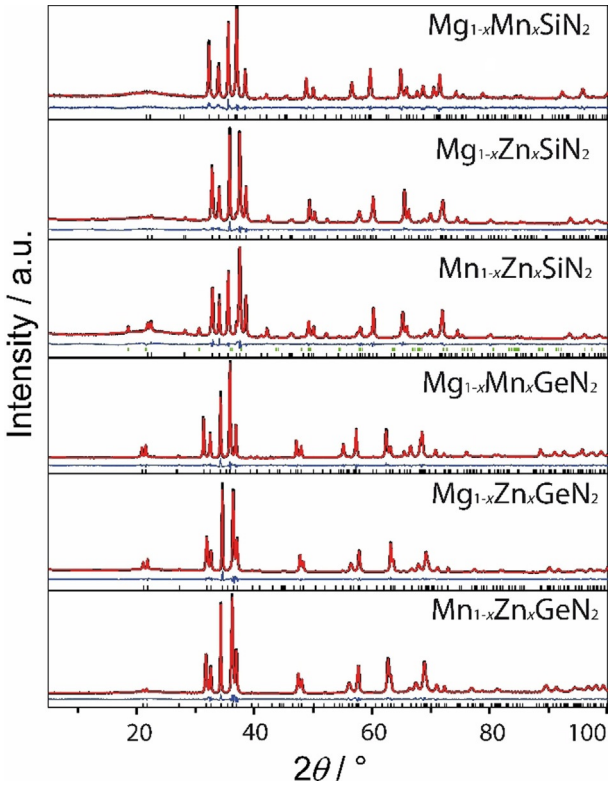

Figure 2. Rietveld refinement of PXRD patterns of solid solutions of II-IV-N_2 compounds (II = Mg, Mn, Zn; IV = Si, Ge) with experimental data (black lines), calculated data (red lines), difference profiles (blue lines), and reflection positions (black bars). Green bars indicate reflection position of K_3MnO_4 side phase.

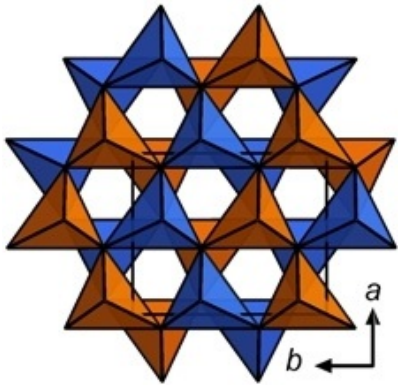

Figure 3. Crystal structure of solid solutions of II-IV-N_2 compounds (II = Mg, Mn, Zn; IV = Si, Ge) along [001]. Mixed occupied II-N_4 tetrahedra are depicted in blue and IV-N_4 tetrahedra in orange.

all other compounds are in the range of ±0.05. The chemical compositions of the products were verified by elemental analysis (see below). Cell volumes of the solid solutions are within the range of those of the respective boundary phases reported in the literature.[11–12] However, the values of the solid solution deviate slightly from those expected from Vegard's rule (see Supporting Information Figure S1).[22] Possible explanations for this slight divergence could be a certain heterogeneous phase width of the solid solutions, which could also explain slight reflection broadening in the PXRD patterns of the solid solutions compared to the boundary phases, vacancies in the crystal structure, and measuring inaccuracies.

To show that, in principle, solid solutions with other compositions are possible, $Mg_{1-x}Zn_xGeN_2$ with $x \approx 0.8$ was synthe-

Table 1. Crystallographic data of $Mg_{1-x}Mn_xSiN_2$, $Mg_{1-x}Mn_xGeN_2$, $Mg_{1-x}Zn_xSiN_2$, $Mg_{1-x}Zn_xGeN_2$, $Mn_{1-x}Zn_xSiN_2$, and $Mn_{1-x}Zn_xGeN_2$ ($x \approx 0.5$) obtained by Rietveld refinement.

Formula	$Mg_{1-x}Mn_xSiN_2$ ($x = 0.543$)	$Mg_{1-x}Mn_xGeN_2$ ($x = 0.625$)	$Mg_{1-x}Zn_xSiN_2$ ($x = 0.515$)	$Mg_{1-x}Zn_xGeN_2$ ($x = 0.545$)	$Mn_{1-x}Zn_xSiN_2$ ($x = 0.53$)	$Mn_{1-x}Zn_xGeN_2$ ($x = 0.55$)
crystal system	orthorhombic					
space group	$Pna2_1$ (33)					
a [Å]	5.27579(12)	5.50086(8)	5.26264(8)	5.48149(8)	5.26071(10)	5.48798(9)
b [Å]	6.49871(17)	6.65560(11)	6.36667(11)	6.51446(11)	6.35726(15)	6.54510(13)
c [Å]	5.03780(13)	5.22654(8)	5.00805(7)	5.18384(7)	5.04257(11)	5.22186(9)
cell volume [Å^3]	172.725(7)	191.352(5)	167.797(5)	185.110(5)	168.642(6)	187.566(6)
density [g cm^{-3}]	3.732	5.001	3.972	5.286	4.592	5.676
formula units/cell	4					
T [K]	293(2)					
diffractometer	STOE STADI P					
radiation	$Cu_{K\alpha 1}$ ($\lambda = 1.5406$ Å)					
2θ range [°]	$5.0 \leq 2\theta \leq 100$					
profile function	fundamental parameters model					
background function	shifted Chebyshev					
data points	6365	6365	6365	6365	6365	6365
number of reflections	104	116	100	111	101	114
refined parameters	56	51	50	56	64	52
R values	$R_p = 0.0266$ $R_{wp} = 0.0340$ $R_{Bragg} = 0.0191$	$R_p = 0.0342$ $R_{wp} = 0.0452$ $R_{Bragg} = 0.0134$	$R_p = 0.0395$ $R_{wp} = 0.0490$ $R_{Bragg} = 0.0146$	$R_p = 0.0413$ $R_{wp} = 0.0575$ $R_{Bragg} = 0.0158$	$R_p = 0.0339$ $R_{wp} = 0.0419$ $R_{Bragg} = 0.0114$	$R_p = 0.0368$ $R_{wp} = 0.0491$ $R_{Bragg} = 0.0105$
goodness of fit	2.08	2.47	3.07	3.54	2.60	2.47

sized. The Rietveld plot, atomic coordinates, and crystallographic data are given in the Supporting Information (Figure S2, Tables S7 and S8).

Scanning electron microscopy

SEM was conducted for verification of the chemical composition of the solid solutions as well as for examination of crystallite size and morphology. EDX values are summarized in Tables S9 and S10 in the Supporting Information. The slightly differing compositions measured at different measuring points suggest a phase width. A possible explanation could be the different solubilities of the starting materials (Mg, Mn, and Zn) in supercritical ammonia resulting in a varying transport through the autoclave, which could not be prevented completely by the use of Ta liners. Nevertheless, on the basis of the obtained values, it can be assumed that the solid solutions have an atomic ratio of the divalent cations close to 1:1, which is consistent with the findings obtained from Rietveld refinement. Exemplarily, SEM images of $Mn_{1-x}Zn_xSiN_2$ and $Mn_{1-x}Zn_xGeN_2$ (Figure S3 in the Supporting Information) show crystallites with sizes up to several micrometers. The sizes and well-defined crystal faces suggest a solution-based growth mechanism, as already reported for $ZnGeN_2$.[11] SEM images of the Mg-containing compounds only show nanocrystalline products and were therefore not presented in the Supporting Information.

UV/Vis spectroscopy

The optical properties of the solid solutions were investigated by diffuse reflectance spectroscopy. Whereas the Si compounds show absorption bands in the region between 200 and 350 nm, the absorption bands of the Ge compounds are shifted to higher wavelengths between 300 and 500 nm (see Figure S4 in the Supporting Information). In the case of Mn-containing compounds, sub-bandgap absorption was observed. These absorption bands can be attributed to the absorption of Mn^{2+} [transition of the ground state $^6A_1(^6S)$ to the excited states $^4T_1(^4G)$, $^4T_2(^4G)$, $^4A_1$,$^4E(^4G)$, $^4T_2(^4D)$ and $^4E(^4D)$] according to the literature.[8,23] In the case of the germanium compounds, these absorption bands are partially overlaid by the bandgap absorption.

The Kubelka–Munk function $F(R)=(1-R)^2/2R$, where R is reflectance, was used to calculate pseudo-absorption spectra.[24] Figure 4 shows Tauc plots, which were used for evaluation of the bandgaps E_g, whereby the energy $h\nu$ was plotted against $[F(R)h\nu]^{1/n}$ with $n=1/2$ for direct bandgaps.[25] Direct transitions were assumed according to DFT calculations (see below).

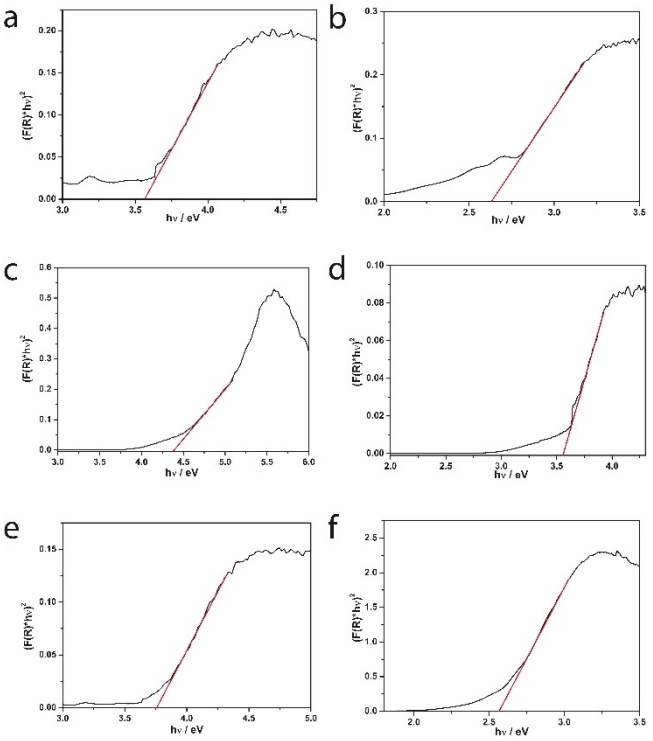

Figure 4. Tauc plots of $Mg_{1-x}Mn_xSiN_2$ (a), $Mg_{1-x}Mn_xGeN_2$ (b), $Mg_{1-x}Zn_xSiN_2$ (c), $Mg_{1-x}Zn_xGeN_2$ (d), $Mn_{1-x}Zn_xSiN_2$ (e), and $Mn_{1-x}Zn_xGeN_2$ (f) with $x\approx0.5$. Red lines indicate tangents at the inflection points.

Table 2 summarizes the measured bandgaps. The evaluated bandgaps are in similar ranges to those already described in the literature for the boundary phases.[9,11,12,26–31] Compared with the boundary phases prepared by ammonothermal syntheses (Figure S5 in the Supporting Information), the measured E_g values of the mixed phases do not exactly match the mean values of their constituent boundary phases.

This is in line with the aforementioned minor deviations and possible measuring inaccuracies of lattice parameters observed from structure refinement. Considering the extensive Urbach tailing observed in the diffuse reflectance spectra (see Figure S4 in the Supporting Information), such deviations may well be explained by slight variations in the occupation of the divalent cation sites, possible defect sites, or resulting increased phonon-assisted absorption in the nanocrystallites obtained from ammonothermal synthesis.[17,32] In the case of $Mg_{1-x}Zn_xGeN_2$ the evaluated bandgap (3.5 eV) is larger than those of the corresponding boundary phases (both 3.2 eV). On the basis of numerous theoretical calculations, it can be assumed that the bandgap of $MgGeN_2$ should actually be larger (around 4 eV) than previously estimated (3.2 eV).[12,33]

Table 2. Evaluated optical bandgaps E_g^{exp} of the mixed-occupancy $(II^a_{1-x}II^b_x)$-IV-N_2 ($x\approx0.5$) compound series from Tauc plots at room temperature and optical bandgaps E_g^{JD} of the mixed-occupancy $(II^a_{0.5}II^b_{0.5})$-IV-N_2 compound series from joint DOS calculations based on the EV-PBE functional within the Munich SPRKKR program package.

	$Mg_{1-x}Mn_xSiN_2$	$Mg_{1-x}Mn_xGeN_2$	$Mg_{1-x}Zn_xSiN_2$	$Mg_{1-x}Zn_xGeN_2$	$Mn_{1-x}Zn_xSiN_2$	$Mn_{1-x}Zn_xGeN_2$
E_g^{exp} ($x\approx0.5$)	3.6 eV	2.7 eV	4.4 eV	3.5 eV	3.8 eV	2.6 eV
E_g^{JD} ($x=0.5$)	3.4 eV	2.8 eV	4.9 eV	4.3 eV	3.4 eV	2.5 eV

DFT calculations

To validate and investigate the observed trends of the experimentally deduced bandgaps of the examined solid solutions, DFT calculations were carried out for all boundary phases and the solid solutions $Mg_{0.5}Mn_{0.5}SiN_2$, $Mg_{0.5}Zn_{0.5}SiN_2$ and $Mn_{0.5}Zn_{0.5}SiN_2$, as well as the isotypical Ge series $Mg_{0.5}Mn_{0.5}GeN_2$, $Mg_{0.5}Zn_{0.5}GeN_2$, and $Mn_{0.5}Zn_{0.5}GeN_2$, in which the mixed occupancy was fixed at 0.5 for the sake of consistency. Each mixed-occupancy model was constructed from a symmetrized average of three VASP-relaxed orderings with regard to atomic position and lattice parameters (for models, see Figure S6 in the Supporting Information).

These pseudorelaxed models were used as starting points for electronic-structure calculations of the mixed-occupancy models $(II^a_{0.5}II^b_{0.5})$-IV-N_2 by means of the Munich SPRKKR package, which has been shown to be a sensible approach according to our previous work.[17] Figure 5 depicts the calculated

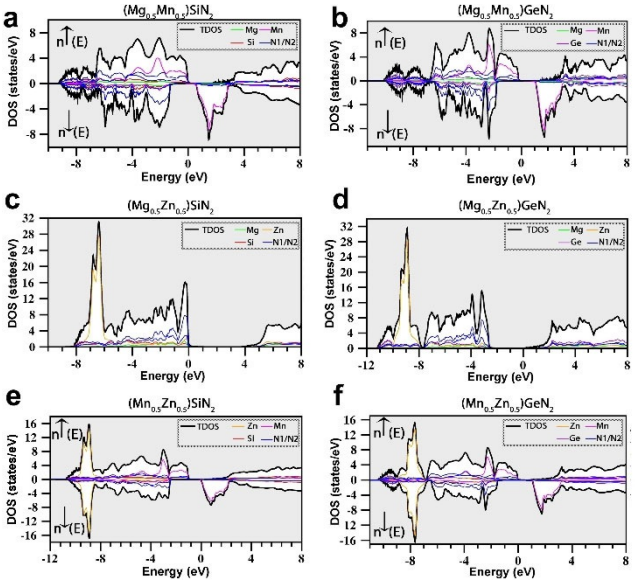

Figure 5. DOS as calculated by the KKR formalism with the coherent potential approximation and Engel–Vosko exchange correlation (EV-GGA) for the mixed-occupancy $(II^a_{0.5}II^b_{0.5})$-IV-N_2 compound series. $(Mg_{0.5}Mn_{0.5})SiN_2$ (a), $(Mg_{0.5}Mn_{0.5})GeN_2$ (b), $(Mg_{0.5}Zn_{0.5})SiN_2$ (c), $(Mg_{0.5}Zn_{0.5})GeN_2$ (d), $(Mn_{0.5}Zn_{0.5})SiN_2$ (e), and $(Mn_{0.5}Zn_{0.5})GeN_2$ (f).

plots of the density of states (DOS) for each material. Excluding temperature effects, all $(Mn_{0.5}II_{0.5})$-IV-N_2 (II = Mg, Zn/IV = Si, Ge) compounds (Figure 5 a, b, e, f) exhibit spin polarization with total magnetic moments ranging between 4.17 and 4.23 μ_B. The obtained electronic bandgaps for the calculated solid solutions lie in between the calculated values of the respective boundary phases for all compounds calculated within the framework of the used code. These obtained E_g values for purely electronic transitions are estimated from the respective Bloch spectral functions (see Figures S7 and S8 in the Supporting Information) and are summarized in Figure 6. For spin-polarized Mn compounds E_g is given in terms of the respective spin-up and spin-down channels along values of magnetic moments. Owing to the underestimation of the exchange correlation by PBE we utilize the EV-PBE functional implemented in SPRKKR to correct the exchange-correlation and increase the bandgap accordingly. For a variety of materials including group 13 nitrides, EV-GGA has been shown to provide accurate band dispersion with gaps lying somewhere between those of LDA/GGA and those from the modified Becke–Johnson (mBJ) potential, the latter of which is widely considered to reproduce gaps with good accuracy.[34–40] Due to the smearing of the bands introduced by the mixed-occupancy disorder and the induced smearing of the Bloch spectral functions, together with the relatively flat progression of the valence states, the assignment of the transition types for the solid solutions is not without ambiguity. For better analysis we performed subsequent calculations on the respective ordering models within VASP and the therein-available mBJ potential. For all ordered compounds $Mg_{0.5}Zn_{0.5}SiN_2$, $Mn_{0.5}Zn_{0.5}SiN_2$, and $Mn_{0.5}Mg_{0.5}SiN_2$, the ordered models suggest that indirect transitions are slightly favored over direct transitions, whereas for $Mn_{0.5}Zn_{0.5}GeN_2$ and $Mn_{0.5}Mg_{0.5}GeN_2$ direct and indirect transitions arise depending on the cation ordering with only $Mg_{0.5}Zn_{0.5}GeN_2$ showing consistent direct transitions. From the respective KKR calculations of the solid solutions indirect transitions are found for the

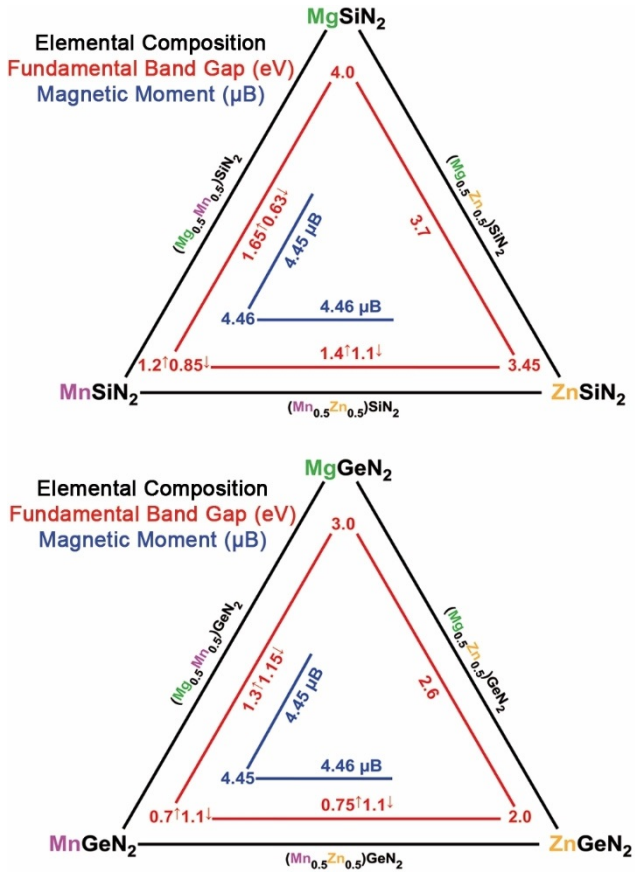

Figure 6. Electronic and magnetic properties as calculated by the KKR formalism with the coherent potential approximation and Engel–Vosko exchange correlation (EV-GGA) for the mixed-occupancy $(II^a_{0.5}II^b_{0.5})$-IV-N_2 compound series. Top: Si series, bottom: Ge series. Arrows indicate direct electronic gaps for up and down spin channels.

$(II^a_{0.5}II^b_{0.5})$-Si-N_2 compounds, albeit with only about 0.05 eV difference to direct transitions. For the $(II^a_{0.5}II^b_{0.5})$-Ge-N_2 compound series, direct and indirect transitions were found to be energetically identical.

As both types of transitions are found for the ordering models, KKR + CPA calculations appear to consistently describe the solid solution for statistical mixed occupancy. With regard to the minimal difference in direct and indirect transitions, we estimate that optically allowed direct transitions are more likely to occur and thus best described with the Kubelka–Munk formalism for direct transitions, as chosen accordingly for the experimental evaluation by UV/Vis spectroscopy.

With regard to the bandgap the ordered mBJ calculations on average further increase the bandgaps from EV-PBE by about 1 eV. Lambrecht et al. have further published a number of computationally dedicated bandgap estimates from QSGW calculations for $MgSiN_2$, $ZnSiN_2$, $MgGeN_2$, and $ZnGeN_2$. For $MgSiN_2$ and $ZnSiN_2$ indirect transitions of 5.84 and 5.44 eV are reported, whereas for $MgGeN_2$ and $ZnGeN_2$ direct transitions of 5.14 and 3.42 eV in magnitude were obtained from the QSGW calculations, respectively, while more recent calculations that explicitly correct the influence of semicore d states suggest a corrected bandgap of 4.11 eV for $MgGeN_2$.[33,41,42]

Although our bandgap determined for $MgGeN_2$ from EV-GGA appears to still underestimate E_g, it seems to be a reasonable cost-efficient correction for the exchange correlation compared to PBE while qualitatively describing the trend in bandgap progression between the II-IV-N_2 boundary phases correctly. Hence, we assume that the fundamental electronic bandgaps of both $(II^a_{0.5}II^b_{0.5})$-Si-N_2 and $(II^a_{0.5}II^b_{0.5})$-Ge-N_2 should be increased by approximately 1 eV, which would place them closer to the QSGW calculations.[33,41,42] A summary of our bandgap determinations, along with experimental and QSGW evaluations from the literature where available, is given in Tables S11 and S12 of the Supporting Information.

Figure 5 shows that the edges of the conduction bands (CBs) for the majority spin channels are characterized by a slow ascent for all II-IV-N_2 compounds. This is due to the limited number of states originating from a single band (conduction band minimum at the Γ point, see also Figure S7 in the Supporting Information), which is mostly characterized by mixed N and M^{2+} states with s character. In turn this implies reduced optical transition probabilities for the optical absorption, as can be seen from calculations of the joint DOS shown in Figure 7. These calculations are in good agreement with the experimentally determined pseudo-absorption spectra from Kubelka–Munk theory, even in terms of analogous bandgap estimates, as shown in Table 2.

Whereas the experimentally determined bandgaps may be lowered due to defects during introduced synthesis and Urbach tail absorptions, the herein-estimated bandgaps from the JDOS are expected to overestimate the fundamental bandgap due to the decreased transition probability of the CB edges. This effect is, however, likely compensated by underestimations for E_g from DFT. The low-energy transitions to the CB at the Γ point seen from the JDOS may also further influence the broad absorption tails observed in the diffuse reflectance spectra. Accordingly, advanced experimental measurement techniques to determine the fundamental bandgaps with more accuracy, such as XAS-XES, may be promising for future investigations of this materials class, which are so far only available for $MgSiN_2$ (XANES-XES: 5.6 eV).[31]

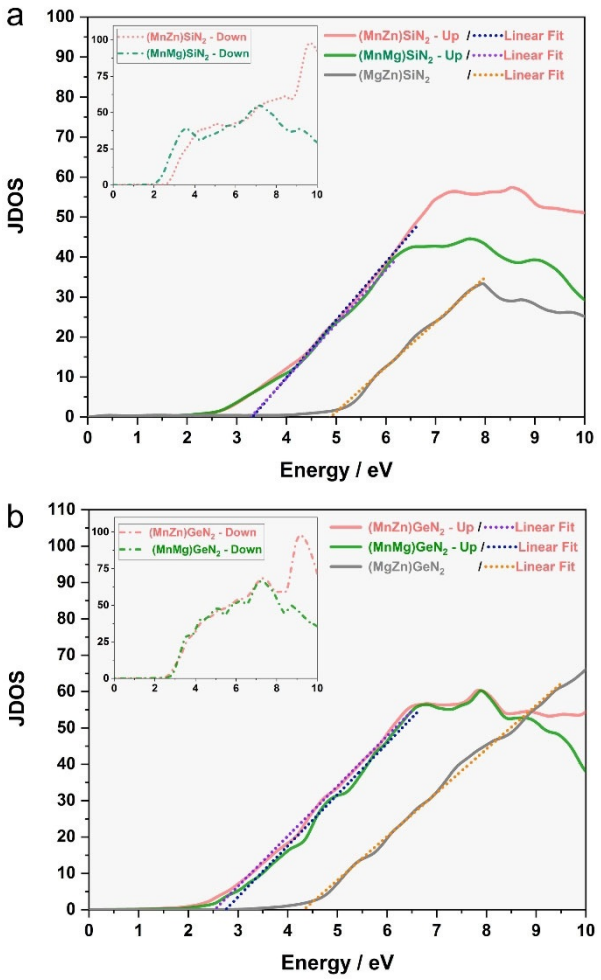

Figure 7. JDOS calculations for $(II^a_{0.5}II^b_{0.5})$-Si-N_2 (a) and $(II^a_{0.5}II^b_{0.5})$-Ge-N_2-compounds (b) within the KKR formalism. Extrapolated linear fits (dotted lines) were used for the estimation of optical band gaps. Inset: JDOS of spin down channels.

Magnetic measurements

Magnetic measurements were performed to investigate the magnetic behavior of the Mn-containing solid solutions. However, due to paramagnetic impurities, a precise statement on the magnetic properties is difficult. A corresponding discussion together with detailed information on the magnetic measurements is presented in the Supporting Information.

Conclusion

We have reported the synthesis of the solid solutions $Mg_{1-x}Mn_xSiN_2$, $Mg_{1-x}Zn_xSiN_2$, $Mn_{1-x}Zn_xSiN_2$, $Mg_{1-x}Mn_xGeN_2$, $Mg_{1-x}Zn_xGeN_2$, and $Mn_{1-x}Zn_xGeN_2$ ($x \approx 0.5$) using supercritical

ammonia (T_{crit} = 405.5 K, p_{crit} = 11.3 MPa) as reaction medium and alkali metal amides as mineralizers.[19] Special autoclaves constructed of nickel-based superalloys (Inconel 718 and Haynes 282) were used for the syntheses. All six compounds crystallize in a wurtzite-type superstructure in space group $Pna2_1$. The measured optical bandgaps range from 2.6 to 3.5 eV (Ge compounds) and 3.6 to 4.4 eV (Si compounds). Additionally, DFT calculations of $(II^a_{0.5}II^b_{0.5})$-IV-N_2 (II = Mg, Mn, Zn; IV = Si, Ge) provided detailed insights into the electronic structures, electronic and optical bandgaps, and type of band transitions. The resulting values for the electronic bandgaps and the values for the optical transitions obtained by JDOS calculations are of the same order of magnitude as the measured ones and thus corroborate the validity of our approach to calculate both solid solutions and boundary phases of II-IV-N_2 semiconductors.

Although the ammonothermal synthesis of ternary and higher (oxide) nitrides is still challenging and only a small number of synthesized compounds are known in the literature, these studies once again demonstrate the great potential of this method.[11–15,43–46] Furthermore, it could be shown within the scope of this work that bandgap tunability is possible in this system, paving the way for possible future applications of bandgap engineering. With regard to the semiconducting properties of II-IV-N_2 and their potential as alternatives to commonly used group 13 nitride semiconductors, the crystal growth and further characterization of materials properties of these solid solutions, for example, electronic band structure measurements by means of XES-XAS measurements, is the next step in the exploration and contribution to a better understanding of II-IV-N_2 compounds.

Experimental Section

The autoclaves were loaded in an Ar-filled glovebox (Unilab, MBraun, Garching, $O_2 < 1$ ppm, $H_2O < 1$ ppm) to prevent contamination with oxygen or moisture. Ammonia was condensed into the autoclaves by using a vacuum line (≤ 0.1 Pa) with argon and ammonia (both: Air Liquide, 99.999%) supply. Gas-purification cartridges (Micro torr FT400-902 (for Ar) and MC400-702FV (for NH_3), SAES Pure Gas Inc., San Luis Obispo, CA, USA) were used for further purification, providing a purity level of <1 ppbV H_2O, O_2, and CO_2.

Ammonothermal synthesis of $Mg_{1-x}Mn_xGeN_2$, $Mg_{1-x}Zn_xGeN_2$, and $Mn_{1-x}Zn_xGeN_2$

$Mg_{1-x}Mn_xGeN_2$, $Mg_{1-x}Zn_xGeN_2$, and $Mn_{1-x}Zn_xGeN_2$ ($x \approx 0.5$) as well as $Mg_{1-x}Zn_xGeN_2$ ($x \approx 0.8$) were synthesized under ammonothermal conditions starting from the corresponding metals [Mg (1.5 mmol, 36.5 mg, Alfa Aesar, 99.8%), Mn (1.5 mmol, 82.4 mg, Alfa Aesar, 99.95%), and Zn (1.5 mmol, 98.1 mg, Alfa Aesar, 99.9%)], Ge (3 mmol, 217.9 mg, smart-elements, 99.99%), and NaN_3 (7.5 mmol, 487.5 mg, Sigma-Aldrich, 99.5%) as mineralizer for $x \approx 0.5$ and Mg (0.75 mmol, 18.2 mg, Alfa Aesar, 99.8%), Zn (2.25 mmol, 147.2 mg, Alfa Aesar, 99.9%), Ge (3 mmol, 217.9 mg, smart-elements, 99.99%), and NaN_3 (7.5 mmol, 487.5 mg, Sigma–Aldrich, 99.5%) for $x \approx 0.8$. The starting materials were mixed and transferred to a Ta liner, to protect the mixture against contamination by the autoclave material. The liners were closed by means of a Ta lid with a small hole. Afterwards, the liner was placed in the autoclave (Inconel 718, max. 900 K, 300 MPa, 10 mL), which was sealed with a lid by means of flange joints with a sealing gasket (silver-coated Inconel 718 ring, GFD seals). The autoclave body is connected via an Inconel 718 high-pressure tube to the upper part, consisting of a hand valve (SITEC), a pressure transmitter (HBM P2VA1/5000 bar), and a bursting disk (SITEC). After closing under argon, the autoclave was evacuated and cooled with an ethanol/liquid nitrogen mixture to 198 K. Subsequently, ammonia (≈ 7 mL) was directly condensed into the autoclave via a pressure regulating valve. The amount of NH_3 was determined by means of a mass flow meter (D-6320-DR, Bronkhorst, Ruurlo, Netherlands). The autoclave was heated to 670 K within 2 h, held at this temperature for 16 h, heated to 870 K within 2 h, and kept at this temperature for 96 h, reaching pressures around 200 MPa. After cooling, residual ammonia was removed and the products were separated in air, washed with EtOH and acetic acid, and dried at 350 K. $Mg_{1-x}Mn_xGeN_2$, $Mg_{1-x}Zn_xGeN_2$ and $Mn_{1-x}Zn_xGeN_2$ ($x \approx 0.5$) were obtained as light brown, beige, and ocher powders, respectively.

Ammonothermal synthesis of $Mg_{1-x}Mn_xSiN_2$, $Mg_{1-x}Zn_xSiN_2$, and $Mn_{1-x}Zn_xSiN_2$

The ammonothermal method was used for synthesis of the solid solutions $Mg_{1-x}Mn_xSiN_2$, $Mg_{1-x}Zn_xSiN_2$, and $Mn_{1-x}Zn_xSiN_2$ ($x \approx 0.5$). The corresponding metals [Mg (1.5 mmol, 36.5 mg, Alfa Aesar, 99.8%), Mn (1.5 mmol, 82.4 mg, Alfa Aesar, 99.95%), and Zn (1.5 mmol, 98.1 mg, Alfa Aesar, 99.9%)], Si (3 mmol, 84.3 mg, Alfa Aesar, 99.9%), and KN_3 (7.5 mmol, 608.4 mg, Sigma-Aldrich, 99.9%) as mineralizer were used as starting materials. Si was ball-milled under argon for 10 h in a planetary ball mill (Retsch PM 400) to support reaction in supercritical ammonia. The reactants were mixed and placed in a Ta liner. The liner was closed by means of a Ta lid with a small hole. Subsequently, the liner was transferred into the autoclave (Haynes 282, max. 1100 K, 170 MPa, 10 mL), which was closed under argon. The autoclave setup was similar to that described above. After evacuating and cooling the reactor to 198 K, NH_3 (≈ 4.5 mL) was condensed into the autoclave. The amount of NH_3 was determined by means of a mass flow meter (D-6320-DR, Bronkhorst, Ruurlo, Netherlands). The autoclave was heated to 670 K over 2 h, held for at that temperature for 16 h, heated to 1070 K within 3 h, and kept at this temperature for 96 h, resulting in maximum pressures of up to 150 MPa. After cooling to room temperature and removing residual ammonia, the samples were extracted from the liners and washed with ethanol and acetic acid. $Mg_{1-x}Mn_xSiN_2$ ($x \approx 0.5$) was obtained as a white powder, and $Mg_{1-x}Zn_xSiN_2$ and $Mn_{1-x}Zn_xSiN_2$ ($x \approx 0.5$) were obtained as brown powders.

Digital microscopy

Optical micrographs of the obtained powders were recorded with a digital microscope (VHX-5000, Keyence) under white-light illumination. All images were collected with a magnification of 200.

Powder XRD

The products were ground and filled in glass capillaries (0.3 mm diameter, 0.01 mm wall thickness, Hilgenberg GmbH). The data were collected with a Stoe STADI P diffractometer with $Cu_{K\alpha1}$ radiation ($\lambda = 1.5406$ Å), Ge(111) monochromator, and Mythen 1K detector in Debye–Scherrer geometry. TOPAS was used for Rietveld refinement.[47]

CCDC 1903084, 1903085, 1903088, 1903087, 1903086, 1903089 ($Mg_{0.375}Mn_{0.625}GeN_2$, $Mg_{0.455}Zn_{0.545}GeN_2$, $Mn_{0.55}Zn_{0.45}GeN_2$, $Mg_{0.457}Mn_{0.543}SiN_2$, $Mg_{0.515}Zn_{0.485}SiN_2$, $Mn_{0.47}Zn_{0.53}SiN_2$) contain the supplementary crystallographic data for this paper. These data are provided free of charge by The Cambridge Crystallographic Data Centre.

Scanning electron microscopy

A Dualbeam Helios Nanolab G3 UC (FEI) scanning electron microscope, equipped with an EDX detector (X-Max 80 SDD, Oxford instruments), was used for determination of crystal morphology and chemical composition. The samples were placed on an adhesive carbon pad and coated with a conductive carbon film by using a high-vacuum sputter coater (BAL-TEC MED 020, Bal Tec A).

UV/Vis spectroscopy

For determination of the optical bandgaps, diffuse reflectance measurements on samples at room temperature were performed with a Jasco V-650 UV/Vis spectrophotometer equipped with Czerny-Turner mount, photomultiplier tube detector, and deuterium (190–350 nm)/halogen (330–900 nm) lamps as light sources.

Computational details

Initial structural relaxations for the ordered models for all $(II^a_{0.5}II^b_{0.5})$-IV-N_2 compounds were performed by means of the VASP program package with the implemented projector augmented wave (PAW) method.[48–52] The generalized gradient approximation (GGA) functional of Perdew, Burke, and Ernzerhof (PBE) was used to model the exchange correlation.[53,54] A plane-wave cutoff energy of 535 eV was used for all calculations together with Brillouin zone sampling on dense gamma-centered Monkhorst–Pack meshes of $10\times8\times10$. Electronic and structural convergence criteria of 10^{-8} and 10^{-7} eV were set in order to ensure precision of total energies. For the respective ordering models the exchange-correlation was further corrected with the modified Becke–Johnson formalism (mBJ-GGA) to estimate the bandgaps more accurately.[40,55,56] Subsequently, to accurately estimate the electronic properties of the experimental solid solution the relaxed structures were averaged, symmetrized, and converted with the CIF2Cell program[57] to formats compatible with the Munich SPRKKR program package.[58,59] The electronic structure was further converged to values of 10^{-5} eV utilizing the implemented fully relativistic Korringa–Kohn–Rostoker (KKR) Green's function method with the PBE functional.[53,54] Owing to the currently missing implementation of the mBJ-GGA potential the EV-GGA (Engel Vosko) formalism was used to obtain more reliable bandgaps by calculating the respective Bloch spectral functions and DOS.[60] The chemical disorder was treated by the coherent potential approximation (CPA) self consistently and fully relativistic within the four-component Dirac formalism. For all calculations an angular momentum expansion of $l=3$ was used.

Acknowledgements

The project was funded by the Deutsche Forschungsgemeinschaft (DFG, German Research Foundation) under Germany's Excellence Strategy—EXC 2089/1-390776260 and within the research group "Chemistry and Technology of the Ammonothermal Synthesis of Nitrides" (FOR 1600), project SCHN377/16-2, by the European Regional Development Fund (ERDF), project CEDAMNF, reg. no. CZ.02.1.01/0.0/0.0/15_003/0000358 and the Czech Science Foundation (GACR), Proj. 17-14840S. The authors gratefully acknowledge the group of Prof. Dr. E. Schlücker (Anna Kimmel and Thomas Steigerwald) for fabrication and maintenance of the autoclaves (FAU Erlangen-Nürnberg). In addition, we want to thank Lisa Gamperl for SEM/EDX measurements and Dr. C. Hoch for digital microscopy pictures (both at Department of Chemistry, LMU Munich).

Conflict of interest

The authors declare no conflict of interest.

Keywords: ammonothermal synthesis · density functional calculations · nitrides · semiconductors · solid solutions

[1] S. P. DenBaars, D. Feezell, K. Kelchner, S. Pimputkar, C.-C. Pan, C.-C. Yen, S. Tanaka, Y. Zhao, N. Pfaff, R. Farrell, M. Iza, S. Keller, U. Mishra, J. S. Speck, S. Nakamura, *Acta Mater.* **2013**, *61*, 945 – 951.
[2] K. Shinohara, D. C. Regan, Y. Tang, A. L. Corrion, D. F. Brown, J. C. Wong, J. F. Robinson, H. H. Fung, A. Schmitz, T. C. Oh, S. J. Kim, P. S. Chen, R. G. Nagele, A. D. Margomenos, M. Micovic, *IEEE Trans. Electron Devices* **2013**, *60*, 2982 – 2996.
[3] J. Wu, W. Walukiewicz, *Superlattices Microstruct.* **2003**, *34*, 63 – 75.
[4] Y. Hinuma, T. Hatakeyama, Y. Kumagai, L. A. Burton, H. Sato, Y. Muraba, S. Iimura, H. Hiramatsu, I. Tanaka, H. Hosono, F. Oba, *Nat. Commun.* **2016**, *7*, 11962.
[5] P. C. Quayle, K. He, J. Shan, K. Kash, *MRS Commun.* **2013**, *3*, 135 – 138.
[6] A. D. Martinez, A. N. Fioretti, E. S. Toberer, A. C. Tamboli, *J. Mater. Chem.* **2017**, *5*, 11418 – 11435.
[7] P. Narang, S. Chen, N. C. Coronel, S. Gul, J. Yano, L. W. Wang, N. S. Lewis, H. A. Atwater, *Adv. Mater.* **2014**, *26*, 1235 – 1241.
[8] S. Esmaeilzadeh, U. Hålenius, M. Valldor, *Chem. Mater.* **2006**, *18*, 2713 – 2718.
[9] C. J. Duan, A. C. A. Delsing, H. T. Hintzen, *J. Lumin.* **2009**, *129*, 645 – 649.
[10] M. Råsander, J. B. Quirk, T. Wang, S. Mathew, R. Davies, R. G. Palgrave, M. A. Moram, *J. Appl. Phys.* **2017**, *122*, 085705.
[11] J. Häusler, S. Schimmel, P. Wellmann, W. Schnick, *Chem. Eur. J.* **2017**, *23*, 12275 – 12282.
[12] J. Häusler, R. Niklaus, J. Minár, W. Schnick, *Chem. Eur. J.* **2018**, *24*, 1686 – 1693.
[13] M. Mallmann, C. Maak, R. Niklaus, W. Schnick, *Chem. Eur. J.* **2018**, *24*, 13963 – 13970.
[14] J. Häusler, L. Neudert, M. Mallmann, R. Niklaus, A.-C. L. Kimmel, N. S. A. Alt, E. Schlücker, O. Oeckler, W. Schnick, *Chem. Eur. J.* **2017**, *23*, 2583 – 2590.
[15] J. Häusler, L. Eisenburger, O. Oeckler, W. Schnick, *Eur. J. Inorg. Chem.* **2018**, 759 – 764.
[16] J. Hertrampf, P. Becker, M. Widenmeyer, A. Weidenkaff, E. Schlücker, R. Niewa, *Cryst. Growth Des.* **2018**, *18*, 2365 – 2369.
[17] R. Niklaus, J. Minár, J. Häusler, W. Schnick, *Phys. Chem. Chem. Phys.* **2017**, *19*, 9292 – 9299.
[18] J. Häusler, W. Schnick, *Chem. Eur. J.* **2018**, *24*, 11864 – 11879.
[19] T. Richter, R. Niewa, *Inorganics* **2014**, *2*, 29 – 78.
[20] The term *sechser* ring was coined by Liebau and is derived from the German word "Sechser"; a *sechser* ring comprises six tetrahedral centers.
[21] E. W. Blanton, K. He, J. Shan, K. Kash, *J. Cryst. Growth* **2017**, *461*, 38 – 45.
[22] A. R. Denton, N. W. Ashcroft, *Phys. Rev. A* **1991**, *43*, 3161 – 3164.
[23] Y. Tanabe, S. Sugano, *J. Phys. Soc. Jpn.* **1954**, *9*, 753 – 766.
[24] R. López, R. Gómez, *J. Sol-Gel Sci. Technol.* **2012**, *61*, 1 – 7.
[25] J. Tauc, R. Grigorovici, A. Vancu, *Phys. Status Solidi B* **1966**, *15*, 627 – 637.
[26] C. M. Fang, R. A. de Groot, R. J. Bruls, H. T. Hintzen, G. de With, *J. Phys. Condens. Matter* **1999**, *11*, 4833 – 4842.
[27] T. Endo, Y. Sato, H. Takizawa, M. Shimada, *J. Mater. Sci. Lett.* **1992**, *11*, 424 – 426.

[28] W. L. Larson, H. P. Maruska, D. A. Stevenson, *J. Electrochem. Soc.* **1974**, *121*, 1673 – 1674.
[29] T. Misaki, A. Wakahara, H. Okada, A. Yoshida, *Phys. Status Solidi C* **2003**, *0*, 2890 – 2893.
[30] M. Shang, J. Wang, J. Fan, H. Lian, Y. Zhang, J. Lin, *J. Mater. Chem. C* **2015**, *3*, 9306 – 9317.
[31] T. de Boer, T. D. Boyko, C. Braun, W. Schnick, A. Moewes, *Phys. Status Solidi RRL* **2015**, *9*, 250 – 254.
[32] E. F. Schubert, *Light-Emitting Diodes*, Cambridge University Press, Cambridge, **2006**.
[33] S. Lyu, W. R. L. Lambrecht, *Solid State Commun.* **2019**, *299*, 113664.
[34] M. Bilal, I. Ahmad, H. A. R. Aliabad, S. J. Asadabadi, *Comput. Mater. Sci.* **2014**, *85*, 310 – 315.
[35] R. Ali, S. Mohammad, H. Ullah, S. A. Khan, H. Uddin, M. Khan, N. U. Khan, *Phys. B* **2013**, *410*, 93 – 98.
[36] A. Reshak, *Int. J. Electrochem. Sci.* **2013**, *8*, 9371 – 9383.
[37] R. Ahmed, S. J. Hashemifar, H. Akbarzadeh, M. Ahmed, Fazal-e-Aleem, *Comput. Mater. Sci.* **2007**, *39*, 580 – 586.
[38] R. Ahmed, H. Akbarzadeh, Fazal-e-Aleem, *Physica B* **2005**, *370*, 52 – 60.
[39] M. I. Ziane, Z. Bensaad, T. Ouahrani, B. Labdelli, H. B. Nacer, H. Abid, *Mater. Sci. Semicond. Process.* **2013**, *16*, 1138 – 1147.
[40] J. A. Camargo-Martínez, R. Baquero, *Phys. Rev. B* **2012**, *86*, 195106.
[41] A. Punya, W. R. L. Lambrecht, M. van Schilfgaarde, *Phys. Rev. B* **2011**, *84*, 165204.
[42] A. P. Jaroenjittichai, W. R. L. Lambrecht, *Phys. Rev. B* **2016**, *94*, 125201.
[43] N. Cordes, W. Schnick, *Chem. Eur. J.* **2017**, *23*, 11410 – 11415.
[44] J. Li, T. Watanabe, H. Wada, T. Setoyama, M. Yoshimura, *Chem. Mater.* **2007**, *19*, 3592 – 3594.
[45] T. Watanabe, K. Nonaka, J. Li, K. Kishida, M. Yoshimura, *J. Ceram. Soc. Jpn.* **2012**, *120*, 500 – 502.
[46] T. Toshima, K. Kishida, Y. Maruyama, T. Watanabe, *J. Ceram. Soc. Jpn.* **2017**, *125*, 643 – 647.
[47] A. Coelho, *TOPAS Academic*, *Version 6*, Coelho Software, Brisbane (Australia), **2016**.
[48] G. Kresse, J. Hafner, *Phys. Rev. B* **1993**, *47*, 558 – 561.
[49] G. Kresse, J. Hafner, *Phys. Rev. B* **1994**, *49*, 14251 – 14269.
[50] G. Kresse, J. Furthmüller, *Comput. Mater. Sci.* **1996**, *6*, 15 – 50.
[51] G. Kresse, D. Joubert, *Phys. Rev. B* **1999**, *59*, 1758 – 1775.
[52] P. E. Blöchl, *Phys. Rev. B* **1994**, *50*, 17953 – 17979.
[53] J. P. Perdew, K. Burke, M. Ernzerhof, *Phys. Rev. Lett.* **1996**, *77*, 3865 – 3868.
[54] J. P. Perdew, K. Burke, M. Ernzerhof, *Phys. Rev. Lett.* **1997**, *78*, 1396.
[55] A. D. Becke, E. R. Johnson, *J. Chem. Phys.* **2006**, *124*, 221101.
[56] F. Tran, P. Blaha, *Phys. Rev. Lett.* **2009**, *102*, 226401.
[57] T. Björkman, *Comput. Phys. Commun.* **2011**, *182*, 1183 – 1186.
[58] H. Ebert, et al., The Munich SPR-KKR Package, Version 7.7, http://olymp.cup.uni-muenchen.de/ak/ebert/SPRKKR, **2012**.
[59] H. Ebert, D. Ködderitzsch, J. Minár, *Rep. Prog. Phys.* **2011**, *74*, 096501.
[60] E. Engel, S. H. Vosko, *Phys. Rev. B* **1993**, *47*, 13164 – 13174.

Manuscript received: August 26, 2019
Accepted manuscript online: September 17, 2019
Version of record online: November 7, 2019

